

A Flexible and High-Voltage Internal Tandem Supercapacitor Based on Graphene-Based Porous Materials with Ultrahigh Energy Density

Fan Zhang, Yanhong Lu, Xi Yang, Long Zhang, Tengfei Zhang, Kai Leng, Yingpeng Wu, Yi Huang, Yanfeng Ma, and Yongsheng Chen*

Pursuing higher working voltage and packaged energy density, an internal tandem supercapacitor has been successfully designed and fabricated based on graphene-based porous carbon hybrid material. Compared with the packaged energy density of $27.2 \text{ Wh kg}_{\text{cell}}^{-1}$ and working voltage of 3.5 V using EMIMBF₄ electrolyte for the conventional single-cell supercapacitor, the internal tandem device with the same material achieves a much higher working voltage of 7 V as well as a significantly improved energy density of $36.3 \text{ Wh kg}_{\text{cell}}^{-1}$ (increased by 33%), which is also about 7 times of that of the state-of-art commercial supercapacitors. A flexible internal tandem device is also designed and fabricated and demonstrated similar excellent performance.

1. Introduction

Energy storage has become a global issue in modern society, and searching for novel, environmental-friendly, low-cost, and high-performance energy storage devices is under great demand nowadays.^[1] Supercapacitors,^[2] also known as electrochemical capacitors or ultracapacitors,^[3,4] have attracted significant attention as an important and rapidly growing class of energy storage and delivery devices. Compared with batteries, there are many advantages of supercapacitors, including ultra high power density, long cycle life, fast charge-discharge rate, no memory effects, wide operational temperature range and improved safety.^[5] Thus, they are commonly used in a wide range of applications, such as back-up systems,

consumer electronics, uninterruptible power sources, and hybrid electric vehicles (HEVs), etc.^[6]

Currently, the state-of-art supercapacitors have a single-cell structure with a working voltage ranging typically from 1.0 to 3.5 V, which is limited by the electrolyte and has a great impact for the energy and power densities since both of them are proportional to the square of the working voltage. Thus, it is highly desired to fabricate devices with higher working voltage, as in the cases using organic and ionic liquid electrolyte systems compared with the aqueous systems.^[7] Particularly, using ionic liquids is preferred in terms of both higher voltage (up to $> 3.5 \text{ V}$) and wider working temperature range, due to the advantages of excellent thermal stability, high ionic conductivity, and the properties of being nonvolatile, nonflammable, and nontoxic.^[8,9]

In order to achieve higher voltages that are required by many power devices in practice, another simple and effective approach is to optimize the device configuration, which can be realized by using the internal tandem architecture. Internal tandem supercapacitors (ITSC) consist of two or more pairs of active electrodes with more separators in one device and thus could greatly increase the working voltage in one packaged device and also reduce the packaging cost which generally takes a significant weight fraction ($> 60\%$) of the whole cell. Compared with most cases in practice, where the supercapacitor devices are packed in modules using

F. Zhang, Y. H. Lu, X. Yang, L. Zhang,
T. F. Zhang, K. Leng, Dr. Y. P. Wu, Prof. Y. Huang,
Prof. Y. F. Ma, Prof. Y. S. Chen
Key Laboratory of Functional Polymer Materials
and Centre of Nanoscale Science and Technology
Institute of Polymer Chemistry
College of Chemistry
Nankai University
300071, Tianjin, China
E-mail: yschen99@nankai.edu.cn



DOI: 10.1002/sml.201303240

many externally connected individual devices in series to obtain a high working voltage, the internal tandem architecture would make the increase of external voltage much more convenient and more efficient. Moreover, as the packaged energy density is a more reliable indicator than the energy density of electrode materials for actual applications, the internal tandem cell design is beneficial to increase the packaged energy density, due to the increase of the active material mass proportion of the whole device to 40% of that based on the electrode materials, while the single-cell device only reaches ~30%.^[10] Although this approach is commonly used in fuel cells,^[11–13] it has been studied only in a very few cases of all-solid-state symmetric supercapacitors^[14–16] or aqueous electrolyte supercapacitors,^[7,17] and has not been explored for supercapacitors in organic/ionic liquid electrolyte systems in the literature.

The performance of the electrode active material is the most important factor for the overall device performance. Thus, more desirable active materials have been sought extensively,^[18–21] and particularly for those sp^2 carbon based materials with higher surface area, more preferable pore size distribution and intrinsic conductivity^[22–24] than the conventional activated carbon (AC) which generally has a gravimetric capacitance of only 70–120 $F\ g^{-1}$ in organic electrolytes.^[25–27] Graphene has excellent intrinsic properties such as high conductivity and surface area,^[28–32] which perfectly fits in the requirements for high performance supercapacitor electrode materials. For instance, graphene has been widely employed in hybrid electrode materials such as graphene/metal oxides,^[33–36] graphene/conductive polymers,^[37–40] and graphene/CNTs.^[41–44]

Recently, we have developed a simple and environment-friendly approach to prepare a 3D cross-linked graphene material in large scale.^[23] In this work, combining all these ideas together and using the graphene-based material prepared by a similar approach above as the electrode active material, we have designed and fabricated an internal tandem supercapacitor using 1 M TEABF₄/AN and EMIMBF₄ as the electrolyte system. The ITSCs exhibit a high working voltage up to 7 V, specific capacitance (213 $F\ g^{-1}$ at 1 $A\ g^{-1}$) and a significantly improved packaged energy density (36.3 $Wh\ kg_{cell}^{-1}$ by 33% compared to single-cell device) as well as good rate performance both in EMIMBF₄ and 1 M TEABF₄/AN electrolyte. Furthermore, flexible ITSCs have also been fabricated and demonstrated similar excellent performances.

2. Results and Discussion

2.1. Synthesis of Active Electrode Materials and Their Pore Structure Analysis

First, to obtain a high performance active electrode material, a series of graphene-based porous materials were synthesized using the method we developed recently^[23] starting from the graphene and lignin composites with different graphene oxide (GO)/lignin weight ratios (Detailed in the Experimental section). Scanning electron microscopy (SEM, Figure S1) shows that the morphology of the graphene/lignin hybrid product material becomes looser with an increase of graphene content. Based on the specific surface area (SSA) results (Figure 1a) and conductivity results (Supporting Information, Figure S2) from the nitrogen adsorption/desorption BET analysis and conductivity results, the material a-HTGL24 (from the GO/lignin composite with weight ratio of 1:24) was selected because it has the highest SSA (3026 $m^2\ g^{-1}$) and good conductivity (75 $S\ m^{-1}$). The parameters of SSA and porosity of all products with different GO/lignin ratios are listed in details in Table S1, which could further reveal great changes of the texture properties of the products with the introduction of GO. Overall, the addition of GO makes the pore size distribution of the materials moves to the mesopore range. This is demonstrated clearly in Figure 1b for the product a-HTGL24, where the pores are made of mainly mesopores (3–7 nm), contrary to that for the controlling samples of a-HTGO or a-HTLIG from GO or lignin only, and the commercial AC product RP20. The nitrogen sorption isotherm of a-HTGL24 shown in Figure S3 also reveals the mesoporosity with a type IV characteristic sorption/desorption

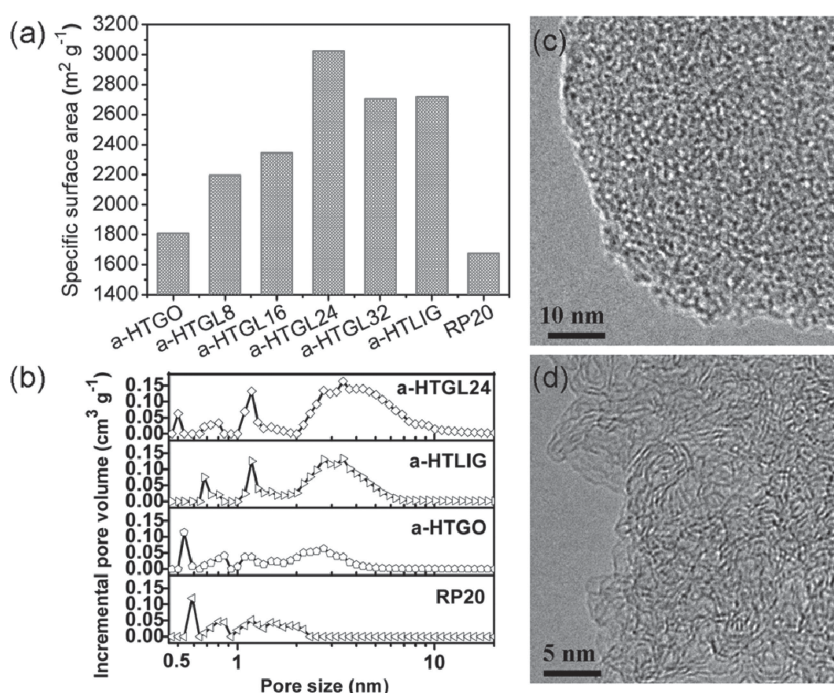


Figure 1. (a) Specific surface areas (SSAs) of graphene/lignin hybrid porous materials in different ratios and commercial AC RP20. The SSA was measured based on the BET method. (b) Pore size distribution for N_2 (calculated using a slit NLDFT model). (c), (d) High resolution TEM images of a-HTGL24.

isotherm of a-HTGL24 shown in Figure S3 also reveals the mesoporosity with a type IV characteristic sorption/desorption

isotherm. Moreover, the morphology of a-HTGL24 that characterized by transmission electron microscopy (TEM) shown in Figure 1c further demonstrates the presence of a dense pore structure, which is composed of abundant pores with 2–3 nm pore size, and the pores are surrounded by highly wrinkled and ridged graphene sheets (Figure 1d). It is expected that the abundant presence of mesopores in a-HTGL24 could facilitate the overall electrolyte ion transportation and interface contact (wetting) between the electrode and the electrolyte ions and thus improve the supercapacitor performance.

2.2. Single-Cell Supercapacitor Device Performance Evaluation

For the purpose of comparison, the performance of conventional single-cell supercapacitor (SCSC) based on the optimized material a-HTGL-24 was evaluated. All electrodes of these materials were made by adding 10 wt% polytetrafluoroethylene (PTFE) as the binder but with no conductive additives, because of the enhanced intrinsic conductivity by graphene introduction for a-HTGL24 (Figure S2, Supporting Information). All electrochemical measurements of the supercapacitor devices were conducted in a symmetrical cell system at room temperature in 1 M TEABF₄/AN and EMIMBF₄ electrolyte respectively, and investigated by standard galvanostatic charge-discharge test, cyclic voltammetry (CV), and electrochemical impedance spectroscopy (EIS).

The performance of the SCSC in EMIMBF₄ electrolyte is shown in **Figure 2**. CV curves shown in Figure 2a exhibit very rectangular shapes from 0 to 3.5 V in a wide range of

scan rates (50–200 mV s⁻¹), indicating an excellent capacitive behavior and rate performance of a-HTGL24 for supercapacitors. Figure 2b shows the galvanostatic charge/discharge curves at different current densities, where the specific capacitance was calculated to be 213, 205, 194 and 183 F/g at current densities of 1, 2, 5 and 10 A g⁻¹ respectively, while the corresponding volumetric capacitance is up to ~66 F cm⁻³ at 1 A g⁻¹. The values of energy density calculated on weight of the active electrode materials follow the same tendency and the highest energy density achieves 90.6 Wh kg⁻¹. For the practical packaged supercapacitor device, the energy density can be estimated to be 30% for the electrode material,^[10] which is about 27.2 Wh kg_{cell}⁻¹ in this case. Figure 2c further summarizes the excellent galvanostatic charge-discharge results of supercapacitor based on a-HTGL24 compared with those based on a-HTGO and a-HTLIG. At the current density of 1 A g⁻¹, the specific capacitance of supercapacitors based on a-HTGL24 exhibits the highest value of 213 F g⁻¹, while a-HTGO device and a-HTLIG device are only 132 F g⁻¹ and 180 F g⁻¹; in addition, the rate performance of a-HTGL24 also shows the best compared to the other two samples. Figure 2d shows the EIS measurement results, where the Nyquist plots of a-HTGO, a-HTLIG and a-HTGL24 are characterized by an inconspicuous semicircular arc in the high frequency region. Compared with the devices from a-HTGO and a-HTLIG prepared from GO or lignin only, the devices from a-HTGL24 prepared from the composite of GO and lignin shows the most vertical curve in the low-frequency region, indicating the best nearly ideal capacitive behavior of the a-HTGL24-based supercapacitor.^[45] The slope of the 45° portion of the curve in the middle frequency range called the Warburg resistance implies the frequency dependence of ion diffusion/transport in the electrolyte.^[46,47] Moreover, the Warburg curve region (inset

in Figure 2d) of a-HTGL24 electrodes is obviously the shortest compared to that of a-HTGO and a-HTLIG in the electrolyte, which is an indication that a-HTGL24 has the shortest ion diffusion path. The excellent SCSC performance of the hybrid material a-HTGL24 is mainly attributed to the high effective specific surface area of this porous hybrid structure with abundant mesopores and its good conductivity with graphene introduction, which both are beneficial to ion diffusion/transport and decrease the resistance of ion traveling at high current densities. The supercapacitors based on a-HTGL24 also show good cycle stability (Supporting Information, Figure S4), which is very important to a supercapacitor for its practical applications. Similar extraordinary SSC performance of a-HTGL24 was also observed in 1 M TEABF₄ electrolyte at 0–2.7 V working voltage, as detailed in Figure S5. All these results indicate that the optimized material a-HTGL24 is a preferable active electrode material for high-performance supercapacitors.

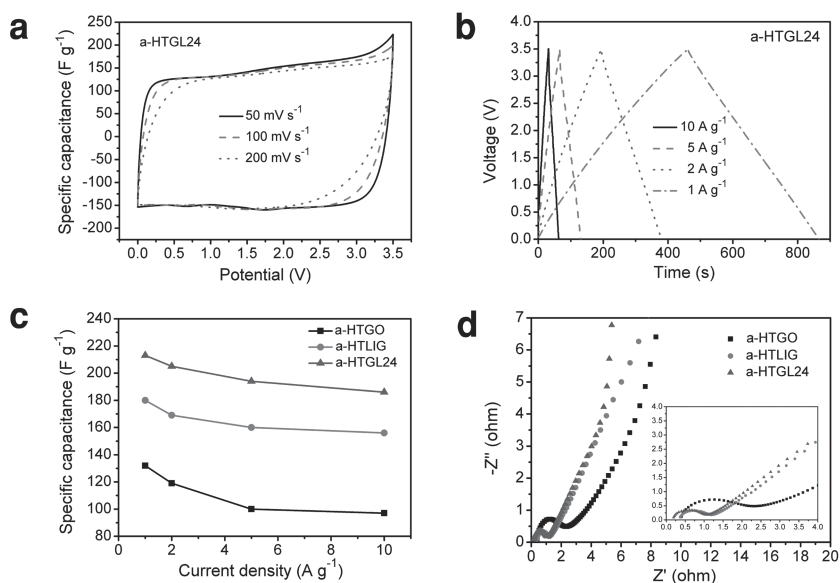


Figure 2. SCSC performances of a-HTGL24 in EMIMBF₄ electrolyte. (a) CV curves with different scan rates. (b) Galvanostatic charge/discharge curves under 1 A g⁻¹, 2 A g⁻¹, 5 A g⁻¹ and 10 A g⁻¹. (c) Galvanostatic charge/discharge testing of a-HTGL24 under 1 A g⁻¹, 2 A g⁻¹, 5 A g⁻¹ and 10 A g⁻¹, with a-HTGO and a-HTLIG for comparison. (d) Nyquist plot of a-HTGO, a-HTLIG and a-HTGL24 based supercapacitors. The inset shows an expanded view for the high-middle frequency range.

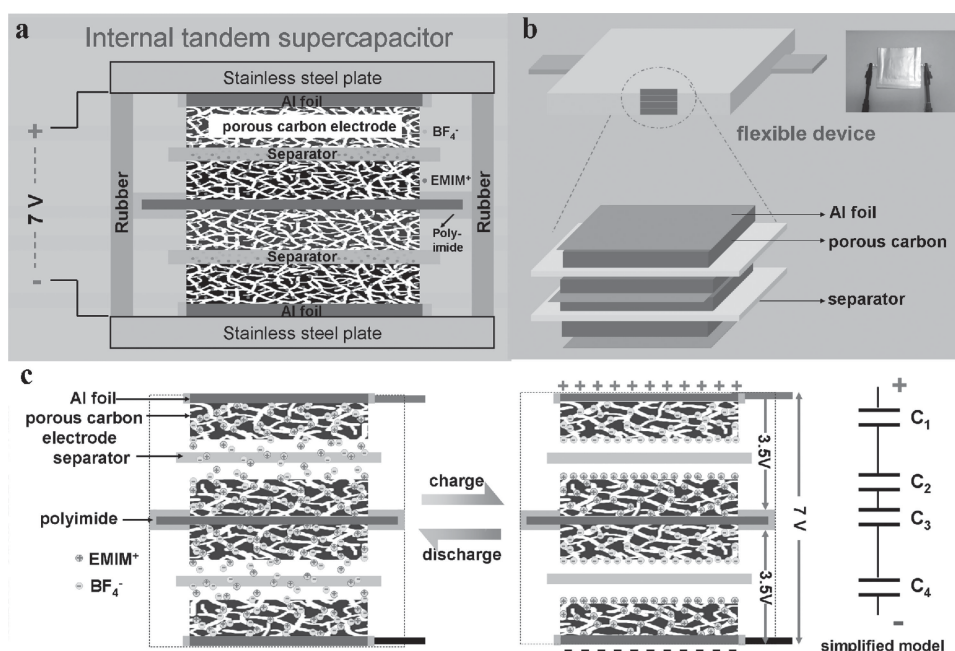


Figure 3. (a) Schematic diagram of ITSC assembly design based on our graphene-based porous material. (b) Structure of flexible ITSC device, inset is the digital image of the device. (c) The working mechanism of ITSC architecture.

2.3. Internal Tandem Supercapacitor Performance

With the optimized material in hand, the internal tandem supercapacitor (ITSC) was designed and fabricated pursuing better performance. The details of fabrication are described in the Experimental section and its structure diagram is displayed in **Figure 3a** and **3b**. All electrochemical performances were measured by a similar method for the SCSC devices above. **Figure 3c** illustrates the working mechanism of ITSC for charge storage and release in higher voltage. In the initial state (left image), cations and anions are distributed disorderly in the system. When the charge process starts, similar to the common SCSC,^[48] cations and anions pass the separators and transport to negative electrode and positive electrode respectively due to the electrostatic physical adsorption (right image). In the middle part of the device, unlike the SCSC device, the additional middle-electrode with double-sides material loading would adsorb opposite ions in each side and separate the device into two electric double-layers, which thus forms the internal tandem state, as seen from the simplified model in **Figure 3c**. When the discharge process starts, electrons flow from the negative electrode to the positive electrode, while cations and anions gradually return back to the electrolyte system, finally the two electric double-layers disappear and recover to the initial state.

The ITSC was evaluated in both 1 M TEABF₄/AN electrolyte and EMIMBF₄ electrolyte, with a double-increased working voltage to 5.4 V and 7 V, respectively, as well as excellent supercapacitor performances, as shown in **Figure 4** and **Figure S6**. It can be clearly seen from **Figure 4a** that at all applied scan rates (50, 100, and 200 mV s⁻¹), the CV plots are semi-rectangular in shape between 0 and 7 V, indicating a closely ideal characteristics of a supercapacitor and also fast electrode kinetics and low internal resistance up to a high

working voltage of 7 V. It is also worthy to point out that using the internal tandem architecture, the applied voltage scan rate can be theoretically shared equally by each unit cell, which is an advantage for an individual cell when fast voltage change and large voltage range are needed in practice.^[7] **Figure 4b** shows the galvanostatic charge/discharge test results at different current densities of 2, 5, 10 A g⁻¹ in 0–7 V, with all the linear profiles of the charge/discharge curves at different current densities and their symmetry. These also reveal the good capacitive performance of the ITSC, which is similar to the SCSC discussed above but at a much higher working voltage. Meanwhile, the calculated specific capacitance of the ITSC still remains almost the same as those based on the SCSC at different current densities, demonstrating the great rate performance can still be kept in the ITSC as well. **Figure 4c** shows the Nyquist plots of the ITSC and the SCSC for comparison. Obviously, both plots show very vertical curves in the low-frequency region, indicating that the ITSC still keeps nearly ideal capacitive behavior. The inset plots give a little larger equivalent series resistance (ESR) equals to 0.91 Ω of ITSC, but still smaller than the double value of that of SCSC (1.12 Ω), indicating a smaller ESR of the internal tandem device than the external tandem device.

The Ragone plots of the packaged energy density vs. power density of the ITSC and SCSC in EMIMBF₄ are shown in **Figure 5a**. For the ITSC devices, the packaged energy density reaches to 36.3 Wh kg_{cell}⁻¹ (at a power density of 305.7 W kg_{cell}⁻¹) in EMIMBF₄, a 33% increase compared with that (27.2 Wh kg_{cell}⁻¹ at a power density of 242.8 W kg_{cell}⁻¹) of the conventional SCSC device, which is mainly due to the increased weight proportion of the electrode material in the whole device. Besides, the packaged energy density of ITSC devices is also about 7 times of that of the commercial

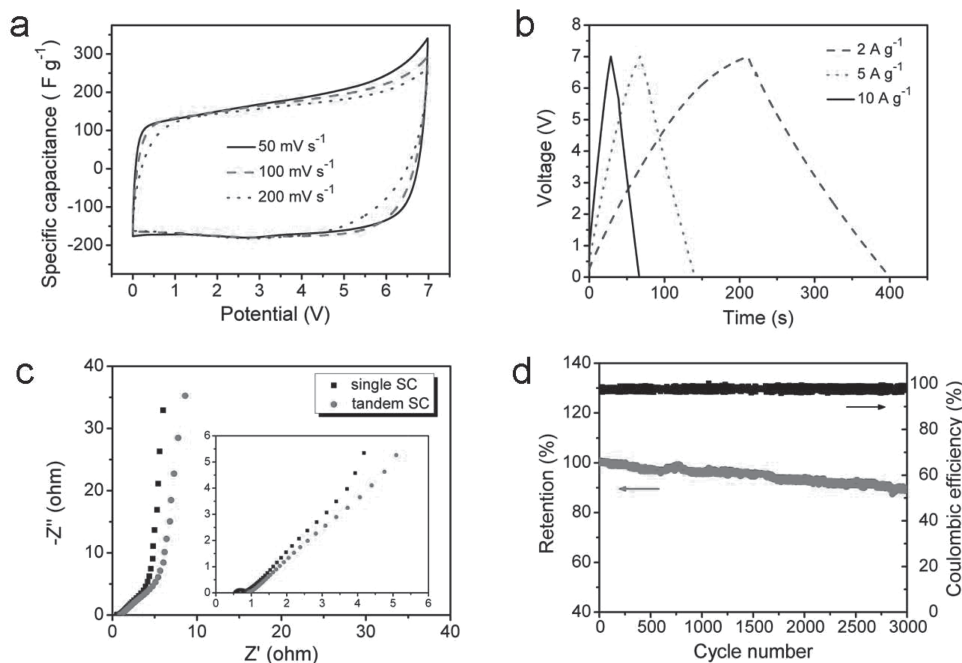


Figure 4. Electrochemical performances of a-HTGL24 based ITSC in EMIMBF₄. (a) CV curves with different scan rates of 50–200 mV s⁻¹ in the potential range of 0–7 V. (b) Galvanostatic charge/discharge test results at different current densities of 2, 5, 10 A g⁻¹ in 0–7 V. (c) Nyquist plots of a-HTGL24 based ITSC and the compared SCSC in the frequency of 100 kHz – 10 mHz. (d) Cycle stability of a-HTGL24 tandem cell over 3000 cycles in EMIMBF₄ at a constant current density of 2 A g⁻¹ in 0–7 V.

single supercapacitor.^[49] Even at a faster charge/discharge rate (10 A g⁻¹, within 66 s fully charged and discharged), the energy density still remains at 29.3 Wh kg_{cell}⁻¹ with a high power density of 4946.0 W kg_{cell}⁻¹. In addition, all these values of the ITSCs are also much higher than the values in the literature for the conventional SCSC devices at similar conditions.^[8,22,43,50]

Our concern using ITSC architecture to achieve higher working voltage and packaged energy density are also applicable to other electrolyte systems and materials. For example, in the 1 M TEABF₄/AN system using the same material a-HTGL24, the packaged energy density of ITSC device can reach up to 19.3 Wh kg_{cell}⁻¹, ~34% increase compared with that (14.4 Wh kg_{cell}⁻¹) of the SCSC device (shown in Figure 5b). In addition, the working voltage can also be double-increased to 0–5.4 V with extraordinary performances such as high

specific capacitance and good rate performance, which is shown in Figure S6. In another case, when the commercial material such as RP20 was used, similar significantly improved performance was achieved as shown in Figure 5b.

In addition, the long-term cycling performance (Figure 4d) still remains at a high retention of 89% after 3000 cycles at 2 A g⁻¹ for a-HTGL24 material in the EMIMBF₄ system, demonstrating good cycle stability even at fast charge/discharge rate and a high working voltage of 7 V. Similar cycling stability was also observed for other materials and electrolyte systems.

2.4. Flexible Internal Tandem Supercapacitor Performance

The flexible internal tandem supercapacitors (FITSC, 1.0 cm × 2.5 cm for each electrode) were further fabricated to show the universality for application of the internal tandem design, as already shown in Figure 3b. **Figure 6** demonstrates the electrochemical performance of FITSC in EMIMBF₄. The CV curves (Figure 6a) and galvanostatic charge/discharge curves (Figure 6b) of FITSC both exhibit the same as those of ITSC, which reflects the stability and universality of the internal tandem architecture. In addition, an FITSC device was placed under various mechanical deformations to evaluate the flexibility and electrochemical performance stability. The CV curves collected at a scan rate of 200 mV s⁻¹ for the FITSC device under different bending angles

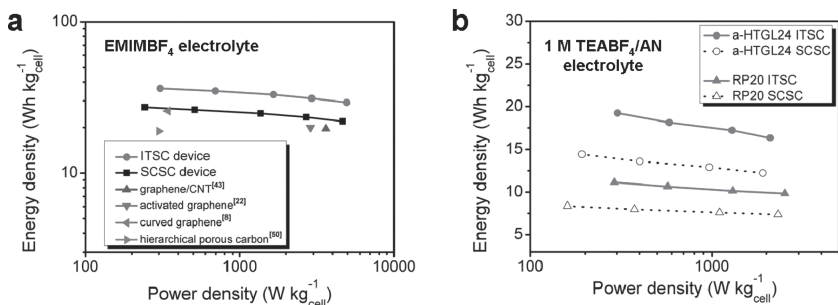


Figure 5. (a) Ragone plot of a-HTGL24 based ITSC and SCSC in EMIMBF₄, with values obtained from common SCSC devices based on various materials in the literature for comparison. (b) Ragone plot of ITSC and SCSC in 1 M TEABF₄/AN based on different electrode materials including a-HTGL24 and RP20. The two Ragone plots indicate the universal performance improvement of the internal tandem design for different electrolytes and materials.

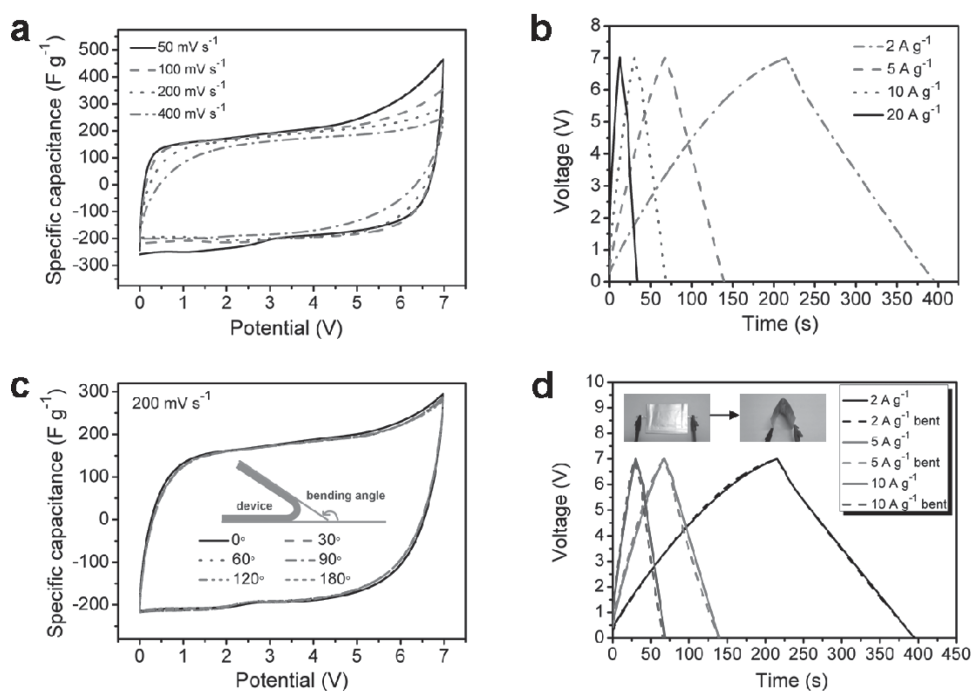


Figure 6. Electrochemical performance of a FITSC in EMIMBF₄. (a) CV curves with different scan rates of 50–400 mV s⁻¹ in the potential range of 0–7 V. (b) Galvanostatic charge/discharge curves at different current densities of 2, 5, 10, 20 A g⁻¹ in 0–7 V. (c) CV curves collected at a scan rate of 200 mV s⁻¹ for the FITSC device under different bending angles. Inset is the schematic of the FITSC device under stress and the bending angle definition. (d) Comparison of galvanostatic charge/discharge curves of FITSC bent before and after. Inset is the digital images of FITSC device showing good flexibility.

(0–180°) have displayed almost similar semi-rectangular shape in Figure 6c, demonstrating that FITSC preserve a constant capacitance output under extreme bending conditions without declining performance.^[51] Furthermore, the galvanostatic charge/discharge curves of FITSC bent before and after almost overlap together at different current densities in Figure 6d, showing the good rate performance preservation at bending condition.

It is worthy to note that the FITSC can be easily scaled up to large-scale production, which is illustrated in Figure S7. The FITSC devices with a-HTGL24 electrodes area of 1.0, 2.5, 5.0, and 10.0 cm² exhibit a capacitance of 0.515, 1.287, 2.558 and 5.157 F at a current density of 2 A g⁻¹, respectively. In addition, the dependence of capacitance values on electrode areas follows a linear relationship, indicating the promising application of fabricating the large-scale FITSC for flexible portable energy storage device in the future.

3. Conclusion

In summary, a novel supercapacitor architecture with internal tandem structure was designed and fabricated, and its packaged energy density increases by ~33% (up to 36.3 Wh kg_{cell}⁻¹) and has a much higher operating voltage window (up to 7 V). This packaged energy density is 7 times that of commercial supercapacitors and equal to that of nickel-metal hydride batteries or lead acid batteries. Furthermore, the tandem devices also demonstrate an excellent cycling stability and rate performance, and this new design is also applicable to different materials and electrolyte systems.

More importantly, similar performances were even observed for the flexible devices based on the internal tandem architecture. Thus, the universal improvement with this new design, together with the same performance for the flexible devices based on the same architecture, is expected to have important implication for the emerging supercapacitor industry and may be applied to other device design.

4. Experimental Section

Materials: Graphite (average particle diameter of 44 μm, 99.95% purity, Qingdao Huarun Graphite Co., Ltd.), lignin (Tianjin Guangfu Chemical Co., Ltd.) and potassium hydroxide (KOH, Wuhan Chujiang Chemical Co., Ltd.) were used as raw materials. Polytetrafluoroethylene (PTFE, solid powder, Dupont), commercial activated carbon RP20 (Kuraray Chemicals), electrolyte 1.0 M tetraethylammonium tetrafluoroborate in AN (TEABF₄/AN, Novolyte) and 1-Ethyl-3-methylimidazolium tetrafluoroborate (EMIMBF₄, Lanzhou Kaite trade Co., Ltd) were all used as purchased. The cellulose film (TF4840, NKK) was used as separator for supercapacitor. Graphite oxide (GO) was prepared using modified Hummers method from flake graphite as previously reported.^[52,53]

Preparation of Graphene-Based Porous Material a-HTGL24: The graphene-based porous materials were prepared as previously reported.^[23] Briefly, lignin aqueous solution (250 mg mL⁻¹) and GO aqueous solution (5 mg mL⁻¹) were homogeneously mixed together with weight ratio of GO to lignin = 1:8, 1:16, 1:24, 1:32, respectively, and transferred to a 100 mL Teflon-lined autoclave. Then, the mixed solution was heated to 180 °C and maintained for 12 h. After cooled down to the room temperature, the solid

product was washed with distilled water and dried in vacuum at 120 °C for 24 h to get the intermediate product. After that, this intermediate product (1 g) was mixed with KOH (4 g) and placed in a horizontal tube furnace, heated up to 800 °C at 5 °C min⁻¹ and kept for 1 h under Ar gas flow. After cooled down to the room temperature, the obtained product was washed with 0.1 M HCl and distilled water until pH = 7. The final product was obtained after dried in vacuum at 120 °C for 24 h, with the name of a-HTGL8, a-HTGL16, a-HTGL24, and a-HTGL32 respectively according to the feed ratio. The product named a-HTGO and a-HTLIG that derived from pure GO and pure lignin respectively were synthesized by the same procedure as controlled materials.

Characterization: Transmission Electron Microscopy (TEM) observation of the material microstructure was carried out using a JEOL TEM-2100 electron microscope. The nitrogen adsorption/desorption analysis was done at 77 K on a Micromeritics ASAP 2020 apparatus. The specific surface area was calculated by the BET method based on adsorption data in the relative pressure (P/P_0) range of 0.05 to 0.3. The total pore volume was measured from the amount of nitrogen adsorbed at a relative pressure (P/P_0) of 0.99. The pore size distribution (PSD) was analyzed using a NL-DFT method with a slit pore model from the nitrogen adsorption data. The electrical conductivity of all the products was tested using the following method. Typically, the sample was mixed with 1 wt.% polytetrafluoroethylene (PTFE, Dupont) as a binder, homogenized, rolled into 100 μm thickness sheet and cut into 3 cm × 1 cm sheet. The resistance (R) of the sheet was tested using a four-probe method, and the electrical conductivity of the film was calculated according to the formula $\lambda = L/(R \times W \times d)$, where λ is the conductivity, L , W , d is the length, width and thickness of the sheet, respectively.

Fabrication of Supercapacitors Based on Porous Material a-HTGL24:

1. All the single supercapacitor devices based on our product a-HTGL24 were fabricated and evaluated by the recommended industry standard method,^[10,54] using the two-electrode system to get reliable performance data. Typically, the final product was mixed with 10 wt% polytetrafluoroethylene (PTFE, solid powder, Dupont) as a binder, and homogenized in an agate mortar. Then it was rolled into 80–100 μm thickness sheets and punched into 12 mm diameter electrodes. The single typical electrode material had a weight between 3.0 and 4.0 mg after dried at 120 °C for 6 h under vacuum. Then two identical (by weight) electrodes were hot pressed onto conductive carbon coated aluminum foils as current collectors and further dried at 180 °C for 6 h. After cooling down to the room temperature, the two electrodes were transferred into a glove box and assembled in a test fixture, which consisted of two current collectors, two electrodes, and an separator (TF4840, NKK) fastened in a fixture with two aluminum plates. The electrolyte was 1 M tetraethylammonium tetrafluoroborate in AN (TEABF₄/AN, Novolyte) which was used as purchased.
2. As a proof of concept, the symmetric internal tandem cell was fabricated based on our a-HTGL24 electrodes that prepared as described above. The cell was assembled in an argon filled glove box in a different configuration. First, the two end electrodes were prepared by one-side loading electrode materials onto conductive carbon coated aluminum foils as described above, then the bipolar electrode in the middle was prepared

similarly by double-sides loading electrode materials onto conductive carbon double-coated aluminum foils. Two separators were settled between the electrodes, and the electric insulation between the two individual symmetric electrode pairs was achieved by sticking polyimide tape around the edge of each electrode (by 2 mm width). Finally the device was infused with 1 M TEABF₄/AN or EMIMBF₄ electrolyte and fastened in a fixture with two aluminum plates and sealed. The loading mass of active materials on each side of electrodes was all the same.

3. The flexible ITSC device was fabricated using a similar method. Each electrode was cut into 1.0 cm × 2.5 cm sheet, and the packed material is soft aluminium foil. The injection of the electrolyte was operated in the glove box after the negative electrode, positive electrode, and separator were assembled together to make the core of FITSC.

Electrochemical Measurements: The electrochemical performance of the single supercapacitor and internal tandem cell based on our product were both studied by galvanostatic charge/discharge test using a supercapacitor tester (Arbin MSTAT, America), while cyclic voltammetry (CV) and electrochemical impedance spectroscopy (EIS) techniques were also carried out using Autolab (Metrohm). CV tests were carried out in various scan rates from 50 mV s⁻¹ to 400 mV s⁻¹ at potential ranges of 0–5.4 V and 0–7 V for single supercapacitor and ITSC respectively. Galvanostatic charge/discharge tests were done in the same potential range at current densities from 1 A g⁻¹ to 20 A g⁻¹, respectively. EIS measurements were carried out at AC amplitude of 10 mV in the range of 100 kHz to 10 mHz. All the electrochemical tests were carried out at room temperature. The gravimetric specific capacitance of the material, C_{sp} (F g⁻¹), was calculated from galvanostatic charge/discharge test according to the formation

$$C_{sp} = \frac{2I}{mdV/dt} \quad (1)$$

where I is the constant current, m is the mass of carbon in each electrode, and dV/dt was calculated from the slope obtained by fitting a straight line to the discharge curve over the range of V (the voltage at the beginning of discharge) to $\frac{1}{2} V$. The energy density based on the total mass of the electrode materials, E (Wh kg⁻¹), was estimated using the formula

$$E = \frac{C_{sp}V^2}{8 \times 3.6} \quad (2)$$

The power density P (W kg⁻¹) was calculated using the formation

$$P = \frac{E}{t} \quad (3)$$

Where E is the energy density (Wh kg⁻¹), and t is the discharge time (s).

Supporting Information

Supporting Information is available from the Wiley Online Library or from the author.

Acknowledgements

The authors gratefully acknowledge financial support from the MoST (2012CB933401 and 2014CB643502), NSFC (Grants 51273093 and 50933003), NSF of Tianjin (10ZCGHHZ00600) and the Synergetic Innovation Center of Chemical Science and Engineering (Tianjin).

- [1] A. S. Arico, P. Bruce, B. Scrosati, J. M. Tarascon, W. V. Schalkwijk, *Nat. Mater.* **2005**, *4*, 366.
- [2] B. E. Conway, *Electrochemical supercapacitors: scientific fundamentals and technological applications*, Plenum, New York, **1999**.
- [3] A. G. Pandolfo, A. F. Hollenkamp, *J. Power Sources* **2006**, *157*, 11.
- [4] M. Winter, R. J. Brodd, *Chem. Rev.* **2004**, *104*, 4245.
- [5] A. Balducci, R. Dugas, P. L. Taberna, P. Simon, D. Plée, M. Mastragostino, S. Passerini, *J. Power Sources* **2007**, *165*, 922.
- [6] J. R. Miller, P. Simon, *Science* **2008**, *321*, 651.
- [7] X. H. Zhou, C. Peng, G. Z. Chen, *AIChE Journal* **2012**, *58*, 974.
- [8] C. Liu, Z. Yu, D. Neff, A. Zhamu, B. Z. Jang, *Nano Lett.* **2010**, *10*, 4863.
- [9] C. Largeot, C. Portet, J. Chmiola, P. L. Taberna, Y. Gogotsi, P. Simon, *J. Am. Chem. Soc.* **2008**, *130*, 2730.
- [10] Y. Gogotsi, P. Simon, *Science* **2011**, *334*, 917.
- [11] M. Hu, S. Sui, X. Zhu, Q. Yu, G. Cao, X. Hong, H. Tu, *Int. J. Hydrogen Energy* **2006**, *31*, 1010.
- [12] N. Rajalakshmi, S. Pandiyan, K. S. Dhathathreyan, *Int. J. Hydrogen Energy* **2008**, *33*, 449.
- [13] C. Lin, L. Huang, L. Chiang, Y. Chyou, *J. Power Sources* **2009**, *192*, 515.
- [14] K. K. Lian, C. Li, R. H. Jung, J. G. Kincs, U.S. Patent 5587872, **1996**.
- [15] P. Staiti, F. Lufano, *J. Electrochem. Soc.* **2005**, *152*, A617.
- [16] A. L. M. Reddy, F. E. Amitha, I. Jafri, S. Ramaprabhu, *Nanoscale Res Lett* **2008**, *3*, 145.
- [17] K. C. Ng, S. Zhang, C. Peng, G. Z. Chen, *J. Electrochem. Soc.* **2009**, *156*, A846.
- [18] L. F. Chen, Z. H. Huang, H. W. Liang, Q. F. Guan, S. H. Yu, *Adv. Mater.* **2013**, *25*, 4746.
- [19] L. Wei, M. Sevilla, A. B. Fuertes, R. Mokaya, G. Yushin, *Adv. Funct. Mater.* **2011**, *22*, 827.
- [20] L. Zhang, F. Zhang, X. Yang, K. Leng, Y. Huang, Y. Chen, *Small* **2013**, *9*, 1342.
- [21] L. Hao, X. Li, L. Zhi, *Adv. Mater.* **2013**, *25*, 3899.
- [22] Y. Zhu, S. Murali, M. D. Stoller, K. J. Ganesh, W. Cai, P. J. Ferreira, A. Pirkle, R. M. Wallace, K. A. Cychoz, M. Thommes, D. Su, E. A. Stach, R. S. Ruoff, *Science* **2011**, *332*, 1537.
- [23] L. Zhang, F. Zhang, X. Yang, G. Long, Y. Wu, T. Zhang, K. Leng, Y. Huang, Y. Ma, A. Yu, Y. Chen, *Sci. Rep.* **2013**, *3*, 408.
- [24] L. Zhang, X. Yang, F. Zhang, G. Long, T. Zhang, K. Leng, Y. Zhang, Y. Huang, Y. Ma, M. Zhang, Y. Chen, *J. Am. Chem. Soc.* **2013**, *135*, 5921.
- [25] P. Simon, Y. Gogotsi, *Nat. Mater.* **2008**, *7*, 845.
- [26] P. L. Taberna, P. Simon, J. F. Fauvarque, *J. Electrochem. Soc.* **2003**, *150*, A292.
- [27] E. Frackowiak, F. Beguin, *Carbon* **2001**, *39*, 937.
- [28] A. K. Geim, *Science* **2009**, *324*, 1530.
- [29] A. K. Geim, K. S. Novoselov, *Nat. Mater.* **2007**, *6*, 183.
- [30] X. Huang, Z. Y. Yin, S. X. Wu, X. Y. Qi, Q. Y. He, Q. C. Zhang, Q. Y. Yan, F. Boey, H. Zhang, *Small* **2011**, *7*, 1876.
- [31] X. Huang, X. Y. Qi, F. Boey, H. Zhang, *Chem. Soc. Rev.* **2012**, *41*, 666.
- [32] Y. Huang, J. Liang, Y. Chen, *Small* **2012**, *8*, 1805.
- [33] S. Chen, J. Zhu, X. Wu, Q. Han, X. Wang, *ACS Nano* **2010**, *4*, 2822.
- [34] J. Yan, Z. Fan, T. Wei, W. Qian, M. Zhang, F. Wei, *Carbon* **2010**, *48*, 3825.
- [35] J. Yan, Z. Fan, W. Sun, G. Ning, T. Wei, Q. Zhang, R. Zhang, L. Zhi, F. Wei, *Adv. Funct. Mater.* **2012**, *22*, 2632.
- [36] X. H. Cao, Y. M. Shi, W. H. Shi, G. Lu, X. Huang, Q. Y. Yan, Q. C. Zhang, H. Zhang, *Small* **2011**, *7*, 3163.
- [37] H. Wang, Q. Hao, X. Yang, L. Lu, X. Wang, *Electrochem. Commun.* **2009**, *11*, 1158.
- [38] J. Xu, K. Wang, S. Z. Zu, B. H. Han, Z. Wei, *ACS Nano* **2010**, *4*, 5019.
- [39] D. W. Wang, F. Li, J. Zhao, W. Ren, Z. G. Chen, J. Tan, Z. S. Wu, I. Gentle, G. Q. Lu, H. M. Cheng, *ACS Nano* **2009**, *3*, 1745.
- [40] S. Bose, N. H. Kim, T. Kaila, K. T. Lau, J. H. Lee, *Nanotechnology* **2011**, *22*, 369502.
- [41] Y. Wang, Y. Wu, Y. Huang, F. Zhang, X. Yang, Y. Ma, Y. Chen, *J. Phys. Chem. C* **2011**, *115*, 23192.
- [42] Y. Wu, T. Zhang, F. Zhang, Y. Wang, Y. Ma, Y. Huang, Y. Liu, Y. Chen, *Nano Energy* **2012**, *1*, 820.
- [43] N. Jha, P. Ramesh, E. Bekyarova, M. E. Itkis, R. C. Haddon, *Adv. Energy Mater.* **2012**, *2*, 438.
- [44] C. Zhang, Z. Peng, J. Lin, Y. Zhu, G. Ruan, C. C. Hwang, W. Lu, R. H. Hauge, J. M. Tour, *ACS Nano* **2013**, *7*, 5151.
- [45] Z. Weng, Y. Su, D. W. Wang, F. Li, J. H. Du, H. M. Cheng, *Adv. Energy Mater.* **2011**, *1*, 917.
- [46] Y. Wang, Z. Q. Shi, Y. Huang, Y. F. Ma, C. Y. Wang, M. M. Chen, Y. S. Chen, *J. Phys. Chem. C* **2009**, *113*, 13103.
- [47] X. Yang, F. Zhang, L. Zhang, T. F. Zhang, Y. Huang, Y. S. Chen, *Adv. Funct. Mater.* **2013**, *23*, 3353.
- [48] A. G. Pandolfo, A. F. Hollenkamp, *J. Power Sources* **2006**, *157*, 11.
- [49] A. D. Pasquier, I. Plietz, S. Menocal, G. Amatucci, *J. Power Sources* **2003**, *115*, 171.
- [50] H. Zhong, F. Xu, Z. Li, R. Fu, D. Wu, *Nanoscale* **2013**, *5*, 4678.
- [51] L. Chen, Z. Huang, H. Liang, Z. Yu, S. Yu, *Energy Environ. Sci.* **2013**, *6*, 3331.
- [52] L. Zhang, J. J. Liang, Y. Huang, Y. F. Ma, Y. Wang, Y. S. Chen, *Carbon* **2009**, *47*, 3365.
- [53] H. A. Becerril, J. Mao, Z. Liu, R. M. Stoltenberg, Z. Bao, Y. Chen, *ACS Nano* **2008**, *2*, 463.
- [54] M. D. Stoller, R. S. Ruoff, *Energy Environ. Sci.* **2010**, *3*, 1294.

Received: October 13, 2013
Revised: November 22, 2013
Published online: February 27, 2014